Journal of Computational Physics 228 (2009) 5628–5649

Contents lists available at ScienceDirect

Journal of Computational Physics

journal homepage: www.elsevier.com/locate/jcp

An investigation of interface-sharpening schemes for multi-phase mixture flows

Daniel A. Cassidy [a], Jack R. Edwards [a,*], Ming Tian [b]

[a] Department of Mechanical and Aerospace Engineering, North Carolina State University, Raleigh, NC 27695-7910, USA
[b] Belcan Corporation, Cary, NC 27511, USA

ARTICLE INFO

Article history:
Received 25 June 2008
Received in revised form 16 February 2009
Accepted 18 February 2009
Available online 5 March 2009

Keywords:
Two-phase flow
Interface-capturing
Incompressible flow

ABSTRACT

This work evaluates several approaches for sharp phase interface-capturing in computations of multi-phase mixture flows. Attention is focused on algebraic interface-capturing strategies that fit directly within a finite-volume MUSCL-type framework, in which dimension-by-dimension reconstruction of interface states based on extrapolated fluid properties is the norm. In this scope, linear, sine-wave, and tangent hyperbola volume-fraction reconstructions are examined for a range of problems, including advection of a volume-fraction discontinuity, the Rayleigh–Taylor instability, a dam-break problem, an axisymmetric jet instability, the Rayleigh instability, and flow within an aerated-liquid injector. An implicit dual-time stepping approach, applied directly to a preconditioned form of the governing equations, is used for time-advancement. The results show that the sharpening strategies are successful in providing two-to-three-cell capturing of volume-fraction discontinuities.

1. Introduction

The development of strategies for sharply capturing the evolution of immiscible, two-phase flows has been an active research area in computational fluid dynamics for decades. Computational strategies have been divided into two main classes: Lagrangian tracking techniques [1–3] and Eulerian capturing methods [4–10], which evolve a marker function to distinguish among the phases. The volume-of-fluid method (VOF) [4–7], in its various forms, offers the possibility of exactly guaranteeing the conservation of mass or volume, at the cost of a significant increase in coding complexity, particularly in three dimensions. Level-set [8–13] methods evolve the signed distance function, instead of a Heaviside marker function, and are thus less susceptible to numerical diffusion errors as the distance function is smooth near the interface. Curvature of the interface can also be calculated more accurately using a level-set approach, and surface-tension effects [9] can be incorporated more precisely as a result. As the distance function does not obey a conservation law, there is no guarantee that mass/volume will be conserved when the level-set function is advected. Complicated re-initialization procedures [9] can reduce these errors to acceptable levels, as can hybrid approaches [10,11] that combine elements of VOF techniques. Ghost-fluid strategies [12–14] have been shown to provide extremely sharp-interface-capturing when used with level-set techniques. More recently, there has been a trend to simplify VOF procedures by introducing smooth basis functions that better represent a discontinuity on the mesh-scale but do not require geometric reconstruction [15–17]. These techniques appear suitable for incorporation into codes that adopt conventional dimension-by-dimension upwinding methods.

Another trend in modern computational fluid dynamics has been the development of flow solvers based on the use of time-derivative preconditioning strategies. If implemented correctly, such techniques offer the potential to extend 'density-based' CFD codes to operate effectively at all flow speeds. At low Mach numbers, the schemes revert to variants

* Corresponding author. Tel.: +1 919 515 5264; fax: +1 919 515 7968.
E-mail addresses: dacassid@unity.ncsu.edu (D.A. Cassidy), jredward@unity.ncsu.edu (J.R. Edwards), ming_tian@gmail.com (M. Tian).

0021-9991/$ - see front matter © 2009 Elsevier Inc. All rights reserved.
doi:10.1016/j.jcp.2009.02.028

of Chorin's artificial compressibility method [18]. If the numerical flux formulae are properly designed, then a discretization suitable for an incompressible flow, with a built-in mechanism for ensuring pressure–velocity coupling, will result [19–21]. These techniques can be extended to multi-phase mixture flows [20,22,23], and calculations for cavitating flows [19–23] and two-flows within 'barbotage' injectors [24,25] have been reported. In a recent study [23], the LDFSS-2001 [19,20] and AUSM+-UP [21] 'all-speed' flux-splitting schemes were compared for a range of problems involving multi-phase mixtures. The performance of the schemes was found to be similar, but a clear need for better phase-interface-capturing was noted in almost all cases. The purpose of this paper is to apply some newer approaches for interface-sharpening to alleviate this problem. The outline of this paper is as follows. First, the governing equations are briefly described, along with a preconditioning strategy for advancing the equations in time. Next, the flux-splitting scheme, higher-order extension, and interface-sharpening schemes used in this investigation are outlined. Details of the time-advancement method are then presented, followed by a discussion of results obtained for several test cases.

2. Governing equations

The governing equations are the incompressible Navier–Stokes equations written for a two-phase mixture as follows:

$$\Omega P\frac{\partial \vec{V}}{\partial \tau}+\frac{\partial \vec{U}}{\partial t}+\sum_k(\vec{E}-\vec{E}_v)_k\cdot\vec{n}_kA_k-\Omega\vec{S}=0 \tag{1}$$

where Ω is the cell volume, $\vec{n}_k$ is an outward-pointing normal vector to face k, and A_k is the area of face k. The inviscid flux vector $\vec{E}_k\cdot\vec{n}_k$ is given as

$$\vec{E}_k\cdot\vec{n}_k=\vec{u}_k\begin{bmatrix}\rho_v\alpha\\ \rho\\ \rho u\\ \rho v\\ \rho w\end{bmatrix}_k+\begin{bmatrix}0\\ 0\\ n_k\\ n_y\\ n_z\end{bmatrix}_k P_k,\quad \vec{n}=n_x\hat{i}+n_y\hat{j}+n_z\hat{k},\quad \hat{u}_k=\vec{u}\cdot\vec{n}=un_x+vn_y+wn_z \tag{2}$$

the conservative variable vector is $\vec{U}=[\rho_v\alpha,\rho,\rho u,\rho v,\rho w]^T$, and the primitive variable vector is $\vec{V}=[\alpha,p,u,v,w]^T$. In this, α is the gas-phase volume fraction, u, v, and w are the Cartesian velocity components, P is the pressure, and the mixture density is defined as $\rho=\rho_v\alpha+\rho_l(1-\alpha)$. The preconditioning matrix is defined as

$$P=\frac{1}{V_{\mathrm{ref},c}^2}\begin{bmatrix}\frac{\rho_v\alpha}{\rho}\\ \rho\\ 1\\ u\\ v\\ w\end{bmatrix}\frac{\partial p}{\partial t}+\frac{\partial \vec{U}}{\partial \vec{V}}=\begin{bmatrix}\rho_v & \frac{1}{V_{\mathrm{ref},c}^2}\frac{\rho_v\alpha}{\rho} & 0 & 0 & 0\\ \rho_v-\rho_l & \frac{1}{V_{\mathrm{ref},c}^2} & 0 & 0 & 0\\ u(\rho_v-\rho_l) & \frac{u}{V_{\mathrm{ref},c}^2} & \rho & 0 & 0\\ v(\rho_v-\rho_l) & \frac{v}{V_{\mathrm{ref},c}^2} & 0 & \rho & 0\\ w(\rho_v-\rho_l) & \frac{w}{V_{\mathrm{ref},c}^2} & 0 & 0 & \rho\end{bmatrix} \tag{3}$$

The eigenvalues of $P^{-1}(\vec{E}\cdot\vec{n})$ are $\vec{u}\cdot\vec{n},\vec{u}\cdot\vec{n},\vec{u}\cdot\vec{n},\frac{1}{2}(\vec{u}\cdot\vec{n}\pm\sqrt{(\vec{u}\cdot\vec{n},)^2+4V_{\mathrm{ref},c}^2})$, where $V_{\mathrm{ref},c}^2$ is a reference velocity to be defined later. It can be seen that this is a form of Chorin's artificial compressibility method [18]. The viscous fluxes are formulated for a Newtonian fluid and are closed by expressing the mixture viscosity as $\mu=\mu_v\alpha+\mu_l(1-\alpha)$. Unless otherwise noted, the phasic densities are set to $\rho_v=1.137\ \mathrm{kg/m^3}$ and $\rho_l=993.5\ \mathrm{kg/m^3}$, the phasic viscosities are set to $\mu_v=1.788\mathrm{e}{-5}\ \mathrm{kg/(m\text{-}s)}$ and $\mu_l=8.564\mathrm{e}{-4}\ \mathrm{kg/(m\text{-}s)}$, and the surface tension is set to 0.072 N/m.

The source vector $\vec{S}$ contains gravitational acceleration terms and a continuum surface force model (CSF). The CSF approach used is the conservative formulation of [26]. Here, the ith component of the CSF is expressed as a surface integral over a mesh cell:

$$\Omega S_i^{\mathrm{csf}}=-\sigma\sum_k|\nabla\alpha|_k(\delta_{ij}-n_in_j)_k\cdot(\hat{n}_j)_kA_k \tag{4}$$

In this expression, the surface tension is α, the normal vector at the phase interface is defined as

$$n_i=\frac{\frac{\partial\alpha}{\partial x_i}}{|\nabla\alpha|},\quad |\nabla\alpha|=\left(\frac{\partial\alpha}{\partial x_i}\cdot\frac{\partial\alpha}{\partial x_i}\right)^{1/2} \tag{5}$$

α is a smoothed volume fraction, and δ_{ij} is the Kronecker delta. In this work, we adopt a simple Jacobi-type smoother involving averaging over nearest neighbors to calculate α. The discretization of the gradient vector at the cell interface is as follows. Given an interface k between two cells i and $i+1$, we first define a vector connecting the cell centers as

$$\vec{\tau}=(x_{i+1}-x_i)\hat{i}+(y_{i+1}-y_i)\hat{j}+(z_{i+1}-z_i)\hat{k} \tag{6}$$

then calculate the gradient at the cell interface by

$$(\nabla\alpha)_k = \left[\overline{\nabla\alpha} - \left(\overline{\nabla\alpha}\cdot\frac{\vec{\tau}}{|\vec{\tau}|}\right)\frac{\vec{\tau}}{|\vec{\tau}|}\right] + \frac{(\alpha_{i+1}-\alpha_i)}{|\vec{\tau}|}\frac{\vec{\tau}}{|\vec{\tau}|} \tag{7}$$

where

$$\overline{\nabla\alpha} = \frac{1}{2}(\nabla\alpha_i + \nabla\alpha_{i+1}) \tag{8}$$

Cell-centered expressions for $|\nabla\alpha|$ in Eq. (8) are obtained from applying Green's theorem. The interface flux in Eq. (4) is evaluated if $(\nabla\alpha)_k > 0.01/|\vec{\tau}|$ and is set to zero otherwise.

3. Flux-splitting method

The LDFSS-2001 scheme [19,20], simplified for incompressible flows, is used in this investigation. Among other properties, LDFSS-2001 exactly captures a grid-aligned stationary contact discontinuity and contains a mechanism for preserving pressure–velocity coupling at low speeds. The baseline compressible formulation is extended to incompressible flows simply by allowing the physical sound speed to approach infinity. In LDFSS-2001, the interface flux is split into convective and pressure contributions:

$$\vec{E}_{i+1/2}\cdot\vec{n}_{i+1/2} = [\vec{E}_{c,j+1/2}(\vec{V}_{L,i+1/2},\vec{V}_{R,i+1/2})] + \vec{E}_{P,i+1/2}(\vec{V}_{L,i+1/2},\vec{V}_{R,i+1/2})]\cdot\vec{n}_{i+1/2} \tag{9}$$

where

$$\vec{E}_{c,i+1/2}\cdot\vec{n}_{i+1/2} = U^+_{i+1/2}\begin{bmatrix}\rho_v\alpha\\ \rho\\ \rho u\\ \rho v\\ \rho w\end{bmatrix}_L + U^-_{i+1/2}\begin{bmatrix}\rho_v\alpha\\ \rho\\ \rho u\\ \rho v\\ \rho w\end{bmatrix}_R \tag{10}$$

where the L/R notation denotes left and right fluid-property states at the interface. The split velocity components are defined as

$$U^+_{i+1/2} = a_{c,1/2}\left[M^+_L - M_{1/2}\underbrace{\left(1-\frac{P_L-P_R+|P_L-P_R|}{2\rho_L V^2_{\mathrm{ref},c,1/2}}\right)}_{\text{pressure diffusion}}\right] \tag{11}$$

$$U^+_{i+1/2} = a_{c,1/2}\left[M^-_R + M_{1/2}\underbrace{\left(1+\frac{P_L-P_R-|P_L-P_R|}{2\rho_R V^2_{\mathrm{ref},c,1/2}}\right)}_{\text{pressure diffusion}}\right] \tag{12}$$

In this, Van Leer/Liou split Mach number definitions based on the 'numerical speed of sound' $a_{c,1/2}$ are used:

$$M^\pm_{L/R} = \pm\frac{1}{4}(M_{L/R}\pm 1)^2, \quad M_{L/R} = \frac{\hat{u}_{L/R}}{a_{c,1/2}} \tag{13}$$

with the velocity component normal to the interface given as

$$\hat{u}_{L/R} = n_{x,i+1/2}u_{L/R} + n_{y,i+1/2}v_{L/R} + n_{z,i+1/2}w_{L/R} \tag{14}$$

and

$$M_{1/2} = \frac{1}{2}\left[M^+_L - \frac{1}{2}(M_L+|M_L|) - M^-_R + \frac{1}{2}(M_R-|M_R|)\right] \tag{15}$$

The 'numerical speed of sound' is given as

$$a_{c,1/2} = \sqrt{\hat{u}^2_{1/2} + 4V^2_{\mathrm{ref},c,1/2}} \tag{16}$$

Unless indicated differently above, the "1/2" notation represents an arithmetic average of left and right states:

$$[\,]_{1/2} = \frac{1}{2}([\,]_L + [\,]_R) \tag{17}$$

The pressure component of the interface flux is expressed as:

$$E_{p,i+1/2} \cdot \vec{n}_{i+1/2} = \begin{bmatrix} 0 \\ 0 \\ n_x \\ n_y \\ n_z \end{bmatrix} p_{1/2} \tag{18}$$

with the interface pressure defined as

$$p_{1/2} = \frac{1}{2}\left[p_L + p_R + \frac{\hat{u}_{1/2}}{a_{p,1/2}}(p_L - p_R) + \underbrace{\frac{\rho_{1/2} V^2_{\mathrm{ref},p,1/2}}{a_{p,1/2}}(\hat{u}_L - \hat{u}_R)}_{\text{velocity-diffusion}} \right] \tag{19}$$

and the 'numerical sound speed' re-defined as

$$a_{p,1/2} = \sqrt{\hat{u}^2_{1/2} + 4V^2_{\mathrm{ref},p,1/2}} \tag{20}$$

Pressure- and velocity-diffusion mechanisms embedded within the LDFSS-2001 flux are highlighted in Eqs. (11), (12), and (19). As discussed in [23], these terms, in addition to advective upwinding, are the dominant sources of numerical diffusion at low Mach numbers. The pressure-diffusion mechanism acts to preserve pressure–velocity coupling, while the velocity-diffusion mechanism acts as an additional normal stress that also suppresses oscillations in the pressure field. The choice of reference velocity can have a significant impact on the convergence of the dual-time stepping procedure described later and on the accuracy of the obtained solutions. In this work, we use two different definitions, one for the convective flux splitting ($V^2_{\mathrm{ref},c}$) and the other for the pressure flux splitting ($V^2_{\mathrm{ref},p}$). Our prior work [25,27] and that of others [28,14] has shown that for unsteady low Mach number flows, one should choose the reference velocity $V^2_{\mathrm{ref},c}$ such that a local minimum Courant number of unity is maintained:

$$V^2_{\mathrm{ref},c} = \max\left(|\vec{u}|^2_{\max}, \left(\frac{\Delta x_{\min}}{\Delta t}\right)^2 \right) \tag{21}$$

where $\Delta x_{\min}$ is a minimum cell dimension and $|\vec{u}|_{\max}$ is the maximum convective velocity present in the flowfield. The reference velocity used in the pressure flux splitting is defined as

$$V^2_{\mathrm{ref},p} = |\vec{u}|^2_{\max} \tag{22}$$

This definition means that the velocity-diffusion component of the interface pressure will not become excessively large as the time step becomes small.

4. Higher-order extension

The baseline technique for extending the first-order LDFSS-2001 scheme to higher-order spatial accuracy is the Piecewise Parabolic Method of Colella and Woodward [29]. Given that $\vec{V} = [\alpha, p, u, v, w]^T$, we first define left- and right-state interface values $\vec{V}_{L/R,i+1/2}$ by the following algorithm:

$$\begin{aligned} \Delta\vec{V}_i &= \vec{V}_{i+1} - \vec{V}_i \\ S_i &= sgn\left[\frac{1}{2}(\Delta\vec{V}_i + \Delta\vec{V}_{i-1})\right] \min\left(\left|\frac{1}{2}(\Delta\vec{V}_i + \Delta\vec{V}_{i-1})\right|, 2|\Delta\vec{V}_i|, 2|\Delta\vec{V}_{i-1}\right|\right), \quad \Delta\vec{V}_i \times \Delta\vec{V}_{i-1} > 0 \\ &= 0, \quad \text{otherwise} \\ \vec{V}_{L,i+1/2} &= \vec{V}_{R,i+1/2} = \frac{1}{2}(\vec{V}_i + \vec{V}_{i+1}) + \frac{1}{6}(S_i + S_{i+1}) \end{aligned} \tag{23}$$

For sufficiently smooth data, this reduces to a fourth-order averaging operator:

$$\vec{V}_{L,i+1/2} = \vec{V}_{R,i+1/2} = \frac{7}{12}(\vec{V}_i + \vec{V}_{i+1}) - \frac{1}{12}(\vec{V}_{i+2} + \vec{V}_{i-1}) \tag{24}$$

Monotonicity is then enforced by the following algorithm:

$$
\begin{aligned}
&\text{if } sgn[(\vec{V}_{L,i+1/2}-\vec{V}_i)(\vec{V}_i-\vec{V}_{R,i-1/2})]=-1, \text{then}\\
&\quad \vec{V}_{L,i+1/2}=\vec{V}_{R,i-1/2}=\vec{V}_i\\
&\text{else}\\
&\quad C=\vec{V}_{L,i+1/2}-\vec{V}_{R,i-1/2}\\
&\quad D=6\left[\vec{V}_i-\frac{1}{2}(\vec{V}_{L,i+1/2}+\vec{V}_{R,i-1/2})\right]\\
&\quad \text{if}(D>C) \text{ then}\\
&\quad\quad \vec{V}_{R,i-1/2}=3\vec{V}_i-2\vec{V}_{L,i+1/2}\\
&\quad \text{else if}(-C>D) \text{ then}\\
&\quad\quad \vec{V}_{L,i+1/2}=3\vec{V}_i-2\vec{V}_{R,i-1/2}\\
&\quad \text{end if}\\
&\text{end if}
\end{aligned}
\tag{25}
$$

The first 'if' block in Eq. (25) resets the interpolation function to a constant if $\vec{V}_i$ is a local maximum or minimum. The second 'if' block in (25) resets either the left-state value at interface $i+1/2$ or the right-state value at interface $i-1/2$ so that the interpolation parabola that connects the interface states with the state at the cell center is monotonically increasing or decreasing. It is also possible to enforce physical constraints (such as positive pressures and bounded volume fractions) at the cell interfaces by a similar cell-by-cell resetting algorithm. The PPM requires a seven point stencil in each coordinate direction.

5. Sharp-interface-capturing

Bounded downwind differencing schemes, such as CICSAM (compressive interface-capturing scheme for arbitrary meshes) [5] and THINC (tangent of hyperbola for interface-capturing) [16,17], achieve sharp-interface-capturing by introducing a controlled amount of numerical dispersion in the vicinity of phase interfaces. Our attention focuses on algebraic interface-capturing schemes [15–17], which are similar to MUSCL-type reconstruction techniques in that an assumed form for the property variation of the volume fraction within a mesh cell is chosen. These typically do not use geometric reconstruction of the interface within a mesh cell, as is done in classical VOF methods, and as such, they are easier to implement. In THINC, the tangent hyperbola function is used as a model function for a discontinuous volume fraction within a mesh cell. In principle, however, any model function $\alpha(x)$ that can connect two states α_{i-1} and α_{i+1} in a monotone, compact fashion, such that

$$\alpha_i=\frac{1}{\Delta x}\int_{x_{i-1/2}}^{x_{i+1/2}}\alpha(x)\,dx \tag{26}$$

can be used. In this study, we consider several interface-sharpening schemes, constructed using different model functions. A general goal might be to express the interface flux as it is written in Eq. (9), with $\alpha_{R,i-1/2}=\alpha(x_{i-1/2})$ and $\alpha_{L,i+1/2}=\alpha(x_{i+1/2})$, similar to conventional practice for MUSCL TVD schemes. To start, we consider piecewise linear and sine-wave reconstructions of the volume fraction field. These are shown in Fig. 1 for the specific case of $\alpha_{i-1}=0.1$, $\alpha_i=0.3$, $\alpha_{i+1}=0.95$. For the linear and sine-wave reconstructions, we require that the volume fraction distribution within cell i be bounded by the cell-average values α_{i-1} and α_{i+1}:

$$\alpha_i(x)=\alpha_{i-1}+H\left(\frac{x-x_{i-1/2}}{x_{i+1/2}-x_{i-1/2}}-x_i\right)(\alpha_{i+1}-\alpha_{i-1}),\ \text{where} \tag{27}$$

$$
\begin{aligned}
&H(\phi)=0, \quad \phi<0\\
&H(\phi)=\phi, \quad 0\leqslant\phi\leqslant 1\\
&H(\phi)=1, \quad \phi>1
\end{aligned}
\tag{28}
$$

Enforcing Eq. (26) gives a value for x_i. If only information at left and right states is required ($\alpha_{R,i-1/2}=\alpha(x_{i-1/2})$ and $\alpha_{L,i+1/2}=\alpha(x_{i+1/2})$), then it may not be necessary to solve for x_i directly.

The result for the linear model is as follows. Let $\alpha=\frac{\alpha_i-\alpha_{i-1}}{\alpha_{i+1}-\alpha_{i-1}}$ and initially set

$$
\begin{aligned}
&\alpha_{R,i-1/2}=\alpha_{i-1}\\
&\alpha_{L,i+1/2}=\alpha_{i+1}
\end{aligned}
\tag{29}
$$

to provide a downwind difference approximation. The other state is given by the following conditional statements:

$$
\begin{aligned}
&\alpha_{L,i+1/2}=\alpha_{i-1}+\sqrt{2\alpha}(\alpha_{i+1}-\alpha_{i-1}), \quad \text{if } |\alpha|>1\times10^{-10} \quad \text{and } \alpha<0.5\\
&\alpha_{R,i-1/2}=\alpha_{i+1}-\sqrt{2(1-\alpha)}(\alpha_{i+1}-\alpha_{i-1}), \quad \text{if } |\alpha|>1\times10^{-10} \quad \text{and } \alpha\geqslant 0.5
\end{aligned}
\tag{30}
$$

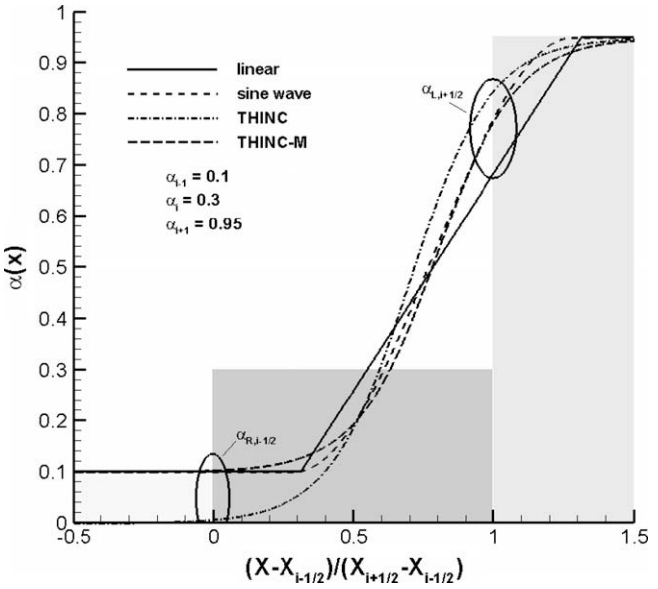

Fig. 1. Volume-fraction reconstruction using several methods.

For the sine-wave discontinuity model,

$$\begin{aligned} &H(\phi) = 0, \quad \phi < 0 \\ &H(\phi) = \frac{1}{2}\left[1 + \sin(\pi(\phi - \frac{1}{2}))\right], \quad 0 \leqslant \phi \leqslant 1 \\ &H(\phi) = 1, \quad \phi > 1 \end{aligned} \tag{31}$$

It is not possible to determine x_i explicitly for this model. Again defining $\alpha = \frac{\alpha_i - \alpha_{i-1}}{\alpha_{i+1} - \alpha_{i-1}}$ and setting $\alpha_{R,i-1/2} = \alpha_{i-1}$, $\alpha_{L,i+1/2} = \alpha_{i+1}$ initially, we curve-fit the transcendental equation that results from satisfying Eq. (26) to yield:

$$\begin{aligned} \alpha_{L,i+1/2} &= \alpha_{i-1} + [1 - (1 - 2\alpha)^{2.0352}]^{0.6356}(\alpha_{i+1} - \alpha_{i-1}), \quad \text{if } |\alpha| > 1 \times 10^{-10} \quad \text{and } \alpha < 0.5 \\ \alpha_{R,i-1/2} &= \alpha_{i+1} - [1 - (2\alpha - 1)^{2.0352}]^{0.6356}(\alpha_{i+1} - \alpha_{i-1}), \quad \text{if } |\alpha| > 1 \times 10^{-10} \quad \text{and } \alpha \geqslant 0.5 \end{aligned} \tag{32}$$

For the THINC model [16], the volume fraction is represented as

$$\alpha_i(x) = \frac{\alpha_{\max}}{2}\left[1 + \gamma \tanh\left(\beta\left(\frac{x - x_{i-1/2}}{x_{i+1/2} - x_{i-1/2}} - x_i\right)\right)\right] \tag{33}$$

where β is chosen as 3.5 in order to localize the discontinuity to approximately one cell. Enforcing Eq. (26) for this model leads to the following procedure for determining left and right states:

$$\begin{aligned} \alpha_{L,i+1/2} &= \frac{1}{2}\alpha_{\max}\left(1 + \gamma\frac{\tanh(\beta) + C}{1 + C\tanh(\beta)}\right) \\ \alpha_{R,i-1/2} &= \frac{1}{2}\alpha_{\max}(1 + \gamma C) \end{aligned} \tag{34}$$

where

$$\begin{aligned} &B = \exp\left[\gamma\beta(2\frac{\alpha_i + \varepsilon}{\alpha_{\max} + \varepsilon} - 1)\right], \quad \varepsilon = 1 \times 10^{-12} \\ &C = (B/\cosh(\beta) - 1)/\tanh(\beta) \end{aligned} \tag{35}$$

and

$$\alpha_{\max}(\alpha_{i+1}, \alpha_{i-1}), \gamma = sgn(\alpha_{i+1} - \alpha_{i-1}) \tag{36}$$

The THINC model is designed to transition the volume fraction between 0 and $\alpha_{\max} = \max(\alpha_{i+1}, \alpha_{i-1})$. If, as in the case shown in Fig. 1, $\min(\alpha_{i+1}, \alpha_{i-1}) > 0$, then the predicted left or right state can be smaller than $\min(\alpha_{i+1}, \alpha_{i-1})$. This does not appear to be a problem when an exact Riemann solution for the traveling volume fraction is used, as in [16] and [17], but

if implemented in a more approximate manner, with $\alpha_{R,i-1/2} = \alpha(x_{i-1/2})$ and $\alpha_{L,i+1/2} = \alpha(x_{i+1/2})$, this can lead to a loss in monotonicity unless 'clipping' of the left-/right-state values is performed. To alleviate this, we re-define the reconstruction function as

$$\alpha_i(x) = \alpha_{\min} + \frac{\alpha_{\max}}{2}\left[1 + \gamma \tanh\left(\beta\left(\frac{x - x_{i-1/2}}{x_{i+1/2} - x_{i-1/2}} - x_i\right)\right)\right] \tag{37}$$

Enforcing Eq. (26) leads to the following algorithm: (referred to as THINC-M (for monotone THINC)):

$$\begin{aligned}
\alpha_{L,i+1/2} &= \alpha_{\min} + \frac{1}{2}\alpha_{\max}\left(1 + \gamma\frac{\tanh(\beta) + C}{1 + C\tanh(\beta)}\right)\\
\alpha_{R,i-1/2} &= \alpha_{\min} + \frac{1}{2}\alpha_{\max}(1 + \gamma C)
\end{aligned} \tag{38}$$

where

$$\begin{aligned}
B &= \exp\left[\gamma\beta\left(2\frac{(\alpha_i - \alpha_{\min} + \varepsilon)}{(\alpha_{\max} + \varepsilon)} - 1\right)\right], \quad \varepsilon = 1 \times 10^{-12}\\
C &= (B/\cosh(\beta) - 1)/\tanh(\beta)
\end{aligned} \tag{39}$$

and

$$\begin{aligned}
\alpha_{\min} &= \min(\alpha_{i+1}, \alpha_{i-1})\\
\alpha_{\max} &= \max(\alpha_{i+1}, \alpha_{i-1}) - \alpha_{\min}\\
\gamma &= sgn(\alpha_{i+1} - \alpha_{i-1})
\end{aligned} \tag{40}$$

Following [16] and [17], one can also determine left/right-state interpolations by considering the integrated average value of the flux of material crossing a cell boundary, rather than just the end-states, in the Riemann solution. This leads to another representation for left and right states, defined as follows using THINC-M:

$$\begin{aligned}
\alpha_{L,i+1/2} &= -\frac{1}{u_{i+1/2}\Delta t}\int_{x_{i+1/2}}^{x_{i+1/2} - u_{i+1/2}\Delta t} \alpha_i(x)\,dx, \quad u_{i+1/2} \geqslant 0\\
\alpha_{R,i+1/2} &= \frac{1}{u_{i+1/2}\Delta t}\int_{x_{i+1/2}}^{x_{i+1/2} - u_{i+1/2}\Delta t} \alpha_{i+1}(x)\,dx, \quad u_{i+1/2} < 0
\end{aligned} \tag{41}$$

Generalizing to an arbitrary cell interface, we have:

$$\begin{aligned}
\alpha_{L,i+1/2} &= \alpha_{\min} + \frac{1}{2}\alpha_{\max}(1 - \gamma D^+)\\
\alpha_{R,i-1/2} &= \alpha_{\min} + \frac{1}{2}\alpha_{\max}(1 + \gamma D^-)
\end{aligned} \tag{42}$$

with

$$\begin{aligned}
D^+ &= \frac{1}{\beta(v_{i+1/2} + \varepsilon)}\ln\left(\cosh(\beta v_{i+1/2}) - \frac{\tanh(\beta) + C}{1 + C\tanh(\beta)}\sinh(\beta v_{i+1/2})\right)\\
D^- &= \frac{1}{\beta(v_{i-1/2} + \varepsilon)}\ln(\cosh(\beta v_{i-1/2}) + C\sinh(\beta v_{i-1/2}))\\
B &= \exp\left[\gamma\beta\left(2\frac{(\alpha_i - \alpha_{\min} + \varepsilon)}{(\alpha_{\max} + \varepsilon)} - 1\right)\right], \quad \varepsilon = 1 \times 10^{-12}\\
C &= (B/\cosh(\beta) - 1)/\tanh(\beta)\\
v_{i+1/2} &= \frac{|\vec{u}_{i+1/2}\cdot\vec{n}_{i+1/2}|\Delta t}{|\Delta\vec{x}_{i+1/2}\cdot\vec{n}_{i+1/2}|}, \quad \Delta\vec{x}_{i+1/2} = \vec{x}_{c,i+1} - \vec{x}_{c,i}
\end{aligned} \tag{43}$$

and

$$\begin{aligned}
\alpha_{\min} &= \min(\alpha_{i+1}, \alpha_{i-1})\\
\alpha_{\max} &= \max(\alpha_{i+1}, \alpha_{i-1}) - \alpha_{\min}\\
\gamma &= sng(\alpha_{i+1} - \alpha_{i-1})
\end{aligned} \tag{44}$$

A similar formulation for the original THINC scheme has been presented in [17]. Note that in this form, the left- and right-state values will be a function of the time step. This model is denoted as THINC-EM (for THINC exact Riemann – monotone) in the discussion that follows. As our implementation of the original THINC does not use the exact Riemann solution, we refer to this implementation as THINC-AR (for THINC approximate Riemann) to avoid confusing the performance of this variant with the more exact reconstruction presented in Refs. [16,17].

All interface-sharpening schemes are implemented with a final step that over-rides the reconstruction procedures if the initial data for, α_i, and α_{i+1} is not monotone:

$$\alpha_{L,i+1/2} = \alpha_{R,i-1/2} = \alpha_i, \quad \text{if } sgn[(\alpha_{i+1} - \alpha_i)(\alpha_i - \alpha_{i-1})] = -1 \tag{45}$$

6. Time-advancement

Except for some pure-advection test cases, the results presented later use a dual-time stepping method to solve Eq. (1). The implicit formulation at a particular sub-iteration k is given as:

$$\left[\Omega\left(\frac{1}{\Delta\tau}P + \frac{3}{2\Delta t}\frac{\partial \vec{U}}{\partial \vec{V}}\right) + \frac{\partial \vec{R}_s}{\partial \vec{V}}\right]^{n+1,k} \Delta\vec{V}^{n+1,k} = -\left[\frac{\Omega}{\Delta t}\left(\frac{3}{2}U^{n+1,k} - 2U^n + \frac{1}{2}U^{n-1}\right) + \left(\sum_k (\vec{E} - \vec{E}_V)_k \cdot \hat{n}_k A_k - \Omega\vec{S}\right)^{n+1,k}\right],$$
$$\vec{V}^{n+1,k+1} = \vec{V}^{n+1,k} + \Delta\vec{V}^{n+1,k} \tag{46}$$

where $\frac{\partial \vec{R}_s}{\partial \vec{V}}$ is the Jacobian of the steady part of Eq. (1). This system is approximately solved using an incomplete LU decomposition strategy at each sub-iteration. Some problems allow the 'freezing' of the Jacobian matrix elements over the duration of the sub-iterations, but in others, a full re-evaluation and re-factorization is required for stability. The elements of $\frac{\partial \vec{R}_s}{\partial \vec{V}}$ are constructed from local Jacobians of the flux formulae. As an example, an approximate linearization of the flux balance $\vec{E}_{i+1/2} \cdot \vec{n}_{i+1/2} - \vec{E}_{i-1/2} \cdot \vec{n}_{i-1/2}$ yields a tri-diagonal structure of the following form:

$$\frac{\partial(\vec{E}_{i+1/2} \cdot \vec{n}_{i+1/2} - \vec{E}_{i-1/2} \cdot \vec{n}_{i-1/2})}{\partial \vec{V}} \Delta V \approx A^-_{i+1/2}\Delta V_{i+1} + (A^+_{i+1/2} - A^+_{i-1/2})\Delta V_i - A^+_{i-1/2}\Delta V_{i-1} \tag{47}$$

As pointed out in [15], the abrupt change in the fluid properties across a sharp interface can lead to a loss of diagonal dominance in this system and to numerical instability. To mitigate this effect, we follow [15] and use instead the linearization

$$\frac{\partial(\vec{E}_{i+1/2} \cdot \vec{n}_{i+1/2} - \vec{E}_{i-1/2} \cdot \vec{n}_{i-1/2})}{\partial \vec{V}} \Delta V \approx A^-_{i+1/2}\Delta V_{i+1} + \frac{1}{2}\left[(A^+_{i+1/2} - A^-_{i-1/2}) + (A^+_{i+1/2} - A^-_{i-1/2})\right]\Delta V_i - A^+_{i-1/2}\Delta V_{i-1} \tag{48}$$

This treatment has been found to be essential to ensure good stability properties, but small time steps are still required for problems with rapidly-propagating interfaces. Typically, a one-to-two order-of-magnitude reduction in the relative residual of the continuity equation (5 to 25 sub-iterations) is required to yield adequate mass conservation. The time step $\Delta\tau$ is set to 5–20 Δt for the calculations presented next.

7. Results

7.1. Advection of discontinuities

Fig. 2 compares predictions of the advection of a square block under the influence of a velocity field $\vec{u} = -1.0\hat{i} - 1.0\hat{j}$ (m/s). Only the vapor mass conservation equation is solved in these calculations. The 1 m × 1 m mesh contains 128 × 128 cells and the square block is initially placed at the center of the mesh. The calculations are evolved for 400 iterations at a CFL number of 0.25 using Huen's method. Six schemes are compared: PPM, linear reconstruction, sine-wave reconstruction, THINC-AR, THINC-M, and THINC-EM, and three contour levels, corresponding to $\alpha = 0.05$, $\alpha = 0.5$, and $\alpha = 0.95$, are shown in the figures. The PPM reconstruction starts to smear the discontinuity, while the others maintain a sharp interface, spread over about two cells. The THINC-AR reconstruction, implemented as described above, distorts the shape of the square. Ref. [16] and [17], however, show that good results can be obtained if THINC-AR is used with the more exact integration scheme of Eq. (41). The predictions provided by the linear reconstruction, sine-wave reconstruction, THINC-M, and THINC-EM are virtually indistinguishable. Maximum and average percentage mass errors for the schemes are shown in Table 1. No mass error (at least to six decimals of precision) is found in the PPM, THINC-M, and THINC-EM results.

Fig. 3 presents a similar comparison for a rotational velocity field $\vec{u} = \sin(x)\cos(y)\hat{i} - \cos(x)\sin(y)\hat{j}$. The computational domain extends from 0 to π in the *X* and *Y-directions* and contains 128 × 128 cells. The initial volume-fraction distribution is a circle of radius $\pi/5$ centered at $X=\pi/2$, $Y=(\pi+1)/5$. The calculations are advanced in time for 2000 iterations at a CFL of 0.25, the velocity field is then reversed, and the calculations continued for 2000 iterations. The expected response is the deformation of the circular interface into a spiral shape and the return of the interface to a circular shape at the end of the integration. Shown in Fig. 2 are the $\alpha = 0.05$, $\alpha = 0.5$, and $\alpha = 0.95$ contours at 2000 and at 4000 time steps. The PPM reconstruction is again excessively diffusive, and the THINC-AR reconstruction results in excessive shedding of 'flotsam' and 'jetsam'. The linear, sine-wave, and THINC-M reconstructions all capture the interface sharply, with 'jetsam' appearing only at the tail of the spiral, but show evidence of 'stair-stepping' along the interface. The THINC-EM reconstruction provides the best results, smoothly capturing the spiral form of the volume-fraction distribution and returning to a circular shape with minimal error (at least visually). Table 1 shows that, with the exception of THINC-AR, the mass error is less than one-half percent and is approximately 0.01% for the PPM and THINC-EM reconstructions.

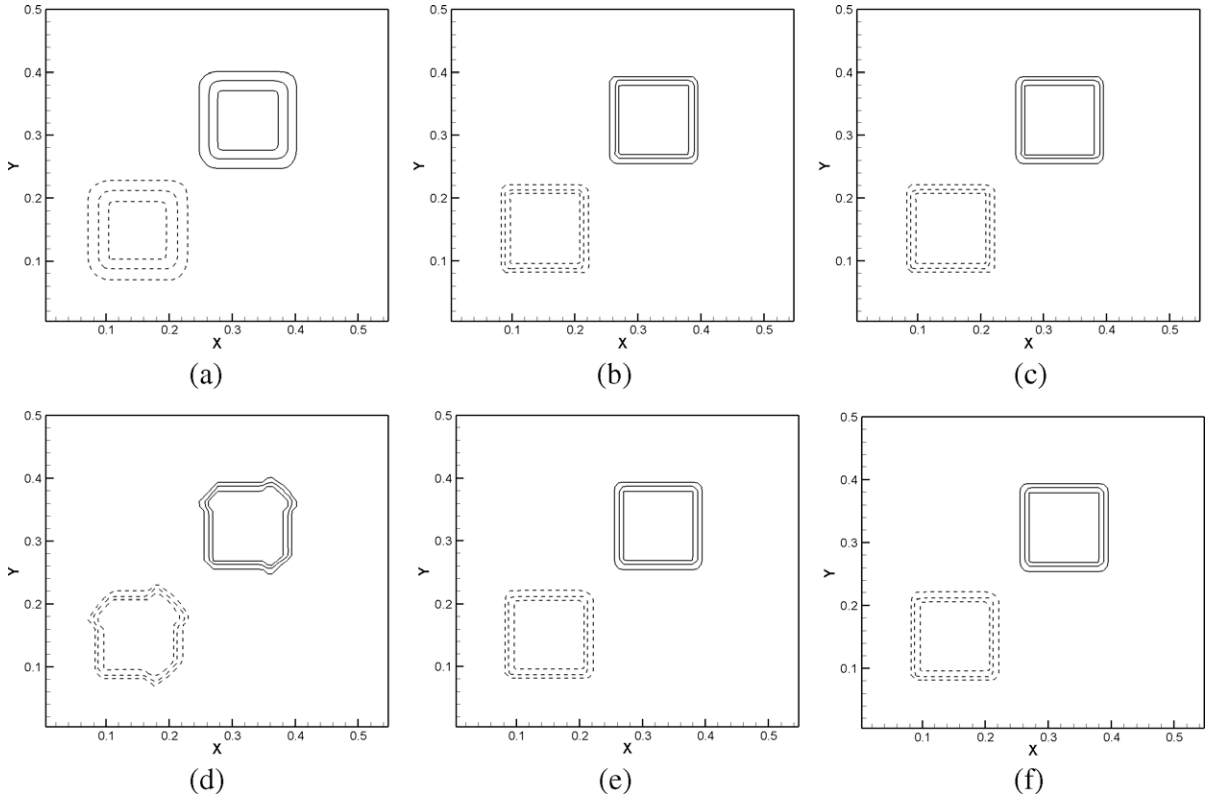

Fig. 2. Advection of a square wave: (a) PPM, (b) linear, (c) sine wave, (d) THINC-AR, (e) THINC-M, (f) THINC-EM) (solid lines: 200 iterations; dashed lines: 400 iterations).

Table 1
Percent mass errors for pure-advection problems.

Scheme	Percent mass error (square)		Percent mass error (rotation)	
	Max	Average	Max	Average
PPM	0.000	0.000	0.010	0.009
Linear	0.005	0.002	0.154	0.098
Sine	0.005	0.002	0.419	0.314
THINC-AR	0.031	0.014	19.156	8.943
THINC-M	0.000	0.000	0.215	0.174
THINC-EM	0.000	0.000	0.012	0.010

Table 2 presents results obtained for Zalesak's notched-disk rotation problem as presented by Yokoi [17]. The two-dimensional computational domain ranges from 0 to 1 in both directions, and three mesh densities (50×50, 100×100, 200×200 cells) are used. The notched circle has a diameter of 0.30 units and is centered at $x = 0.5$ and $y = 0.75$. The notch width and its displacement from the upper edge of the circle are both 0.05 units. The circle is rotated about the point $x = 0.5$, $y = 0.5$. After one rotation at a velocity $\vec{u} = -(y - 0.5)\hat{i} + (x - 0.5)\hat{j}$, the position of the rotated object is compared to the original position, and the error is calculated as

$$\text{Error} = \frac{\sum_{i,j}|\alpha^n_{i,j} - \alpha^0_{i,j}|}{\sum_{i,j}\alpha^0_{i,j}} \tag{49}$$

where the superscript 0 indicates the initial volume-fraction distribution and the superscript n indicates the final time step. A time step of $2\pi/2000$ was used for the 100×100 grid; the time step was doubled for the 50×50 grid and halved for the 200×200 grid. The THINC-M and THINC-EM had the lowest error for each grid size while the PPM had the largest. The trends with mesh refinement are similar to those shown in Ref. [17], though the exact values of the error are different.

7.2. Rayleigh–Taylor instability

A classical test case for two-phase mixture models is the gravity-driven Rayleigh–Taylor instability. Our initial modeling of this problem follows [3,6,11]. The computational domain is a 1 m $\times$ 4 m rectangle discretized into 128×512 cells. The

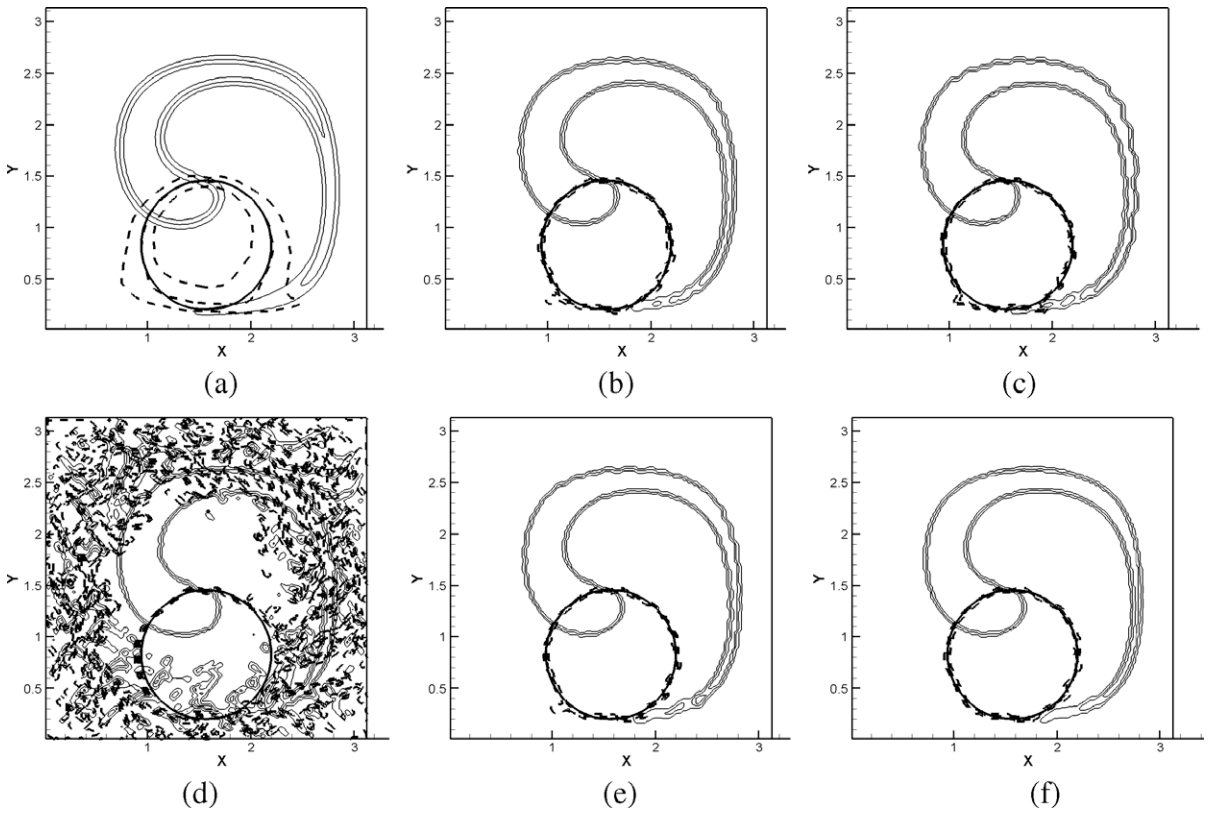

Fig. 3. Distortion of a circle in a rotational velocity field: (a) PPM, (b) linear, (c) sine wave, (d) THINC-AR, (e) THINC-M, (f) THINC-EM) (dark solid black: initial solution; solid black: 2000 iterations; dark dashed black: 4000 iterations).

Table 2
Errors for Zalesak's test problem.

Scheme/grid size	50×50	100×100	200×200
PPM	3.53×10^{-2}	1.80×10^{-2}	9.30×10^{-3}
Linear	1.60×10^{-2}	7.34×10^{-3}	5.73×10^{-3}
Sine	1.51×10^{-2}	6.93×10^{-3}	5.41×10^{-3}
THINC-AR	2.37×10^{-2}	9.54×10^{-3}	4.78×10^{-3}
THINC-M	1.56×10^{-2}	5.60×10^{-3}	2.94×10^{-3}
THINC-EM	1.63×10^{-2}	5.74×10^{-3}	2.94×10^{-3}

interface is described by the function $y(x) = 1.95 + 0.05\cos(2\pi x)$, the density of the heavier fluid is 1.225 kg/m^3, the density of the lighter fluid is 0.1694 kg/m^3, and the viscosity for both fluids is set equal to 0.00313 kg/(m-s). The surface tension is set to zero for these calculations, and the pressure field is in hydrostatic equilibrium. The time step is 0.00125 s, which leads to $\frac{\Delta x_{\min}}{\Delta t}$ equal to 6.25 in Eq. (21). Volume-fraction contours for $\alpha = 0.05$, $\alpha = 0.5$, and $\alpha = 0.95$ are shown at times $t = 2$ s, 7 s, 8 s, and 9 s for THINC-EM in Fig. 4. The predictions compare well with those presented in [3,6] using VOF-type methods. Fig. 5 compares predictions of volume fraction at $t = 12$ s (45 contours, ranging from 0 to 1) for the PPM, linear, THINC-M, and THINC-EM reconstruction methods. The fact that THINC-EM is generally more dissipative than either the linear reconstruction or THINC-M is apparent, as those schemes eventually capture a secondary instability on the liquid jet surface and provide a sharper, though asymmetric rendering of the streak-like structures present as the heavier fluid disperses within the lighter fluid. Table 3 shows the percent mass error for the heavier and lighter fluids. The maximum error occurs just after initialization for all cases and its relatively high value may be due to the process of adjusting the analytic interface profile to a form consistent with the mesh resolution.

Chandrasekhar [30] presented the dimensionless growth rate $n = n^*(\nu/g^2)^{1/3}$ for the Rayleigh–Taylor instability as a function of the dimensionless wave number $k = k^*(\nu^2/g)^{1/3}$, where n^* is the growth rate and k^* is the wave number. The solution is parameterized by the Atwood number $(\rho_2 - \rho_1)/(\rho_2 + \rho_1)$(where $\rho_2 > \rho_1$) with the two fluids having equal kinematic viscosities and neglecting surface tension. An additional set of calculations of the Rayleigh–Taylor instability was performed

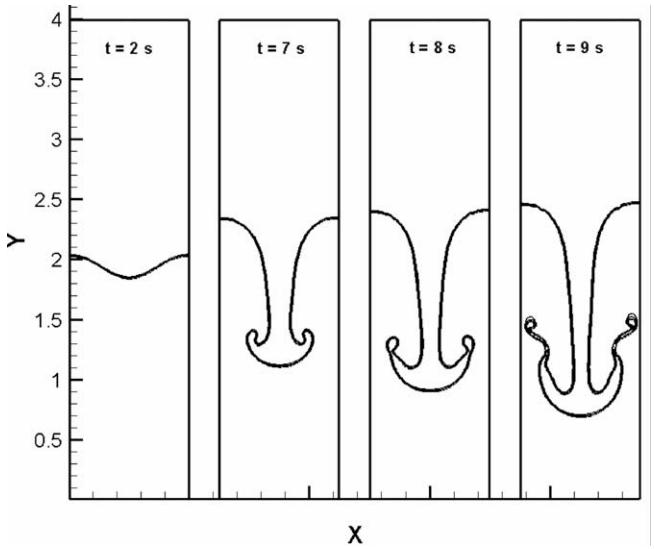

Fig. 4. Evolution of interface in Rayleigh–Taylor instability (THINC-EM).

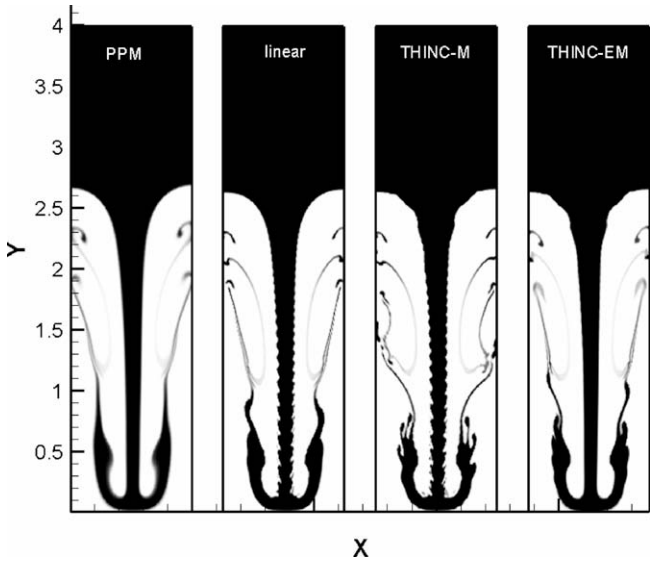

Fig. 5. Evolution of interface in Rayleigh–Taylor instability – effect of reconstruction scheme ($t = 12$ s).

Table 3
Percent mass error for Rayleigh–Taylor instability.

Scheme	Percent mass error (light)		Percent mass error (heavy)	
	Max	Average	Max	Average
PPM	0.252	0.117	0.239	0.112
Linear	0.252	0.095	0.239	0.091
THINC-M	0.252	0.110	0.239	0.105
THINC-EM	0.252	0.089	0.239	0.085

to compare with Chandrasekhar's solution. Following the modeling of Daly [31] and Pan and Chang [15], the interface position is fixed and an initial velocity is assigned to the two fluids as

$$u = \begin{cases} \frac{\pi A \Delta y}{2L} \sin\left(\frac{\pi x}{L}\right) \exp\left(\frac{-\pi|y|}{L}\right) & y > 0 \\ -\frac{\pi A \Delta y}{2L} \sin\left(\frac{\pi x}{L}\right) \exp\left(\frac{-\pi|y|}{L}\right) & y \leqslant 0 \end{cases}, \quad v = \frac{\pi A \Delta y}{2L} \cos\left(\frac{\pi x}{L}\right) \exp\left(\frac{-\pi|y|}{L}\right) \tag{50}$$

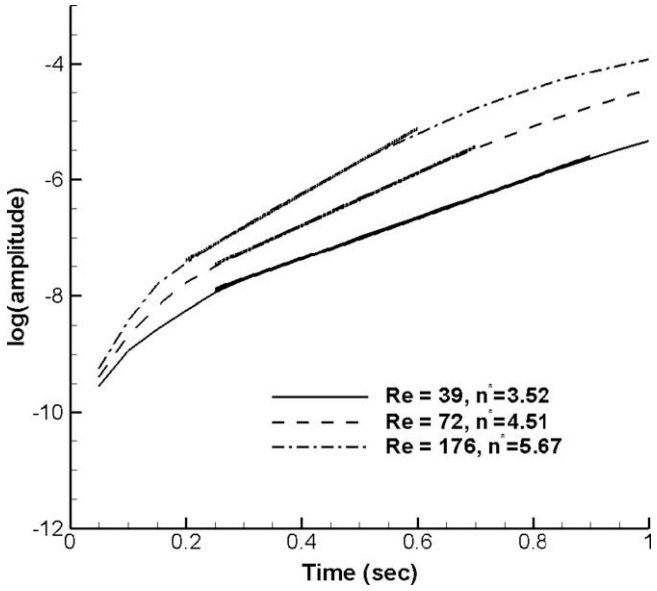

Fig. 6. Disturbance amplitude versus time (Rayleigh–Taylor instability; THINC-EM).

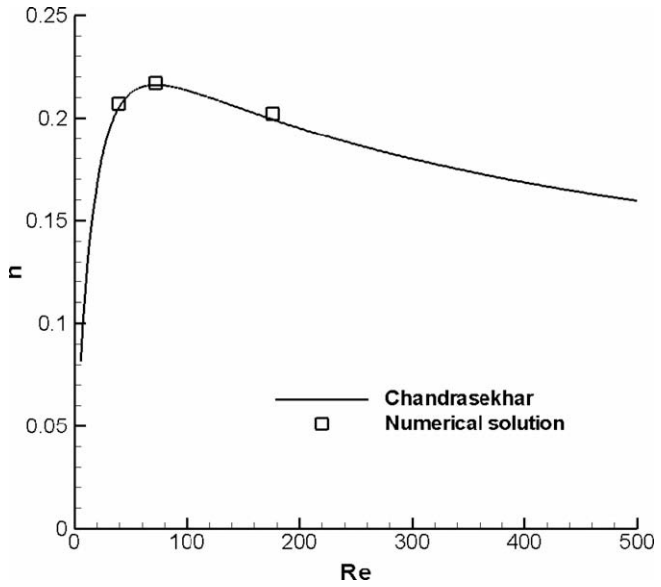

Fig. 7. Dimensionless growth rate versus Reynolds number (Rayleigh–Taylor instability; THINC-EM).

where $\Lambda = 2L$ is the wavelength of the perturbation, A is the amplitude, and Δy is the mesh spacing in the vertical direction. For the case under consideration, $L = 0.02$, $A = 0.1$, $\Delta y = 5 \times 10^{-4}$, the height of the domain is $6L$, the Atwood number is 1/3, the gravitational acceleration is set to unity, and the grid contains 40×120 cells. Three Reynolds numbers were tested, Re = 39, 72, and 176, where the Reynolds number is defined as $Re = \frac{\Lambda^{3/2} g^{1/2}}{\nu}$. Kinematic viscosities corresponding to these Reynolds numbers are $\nu = 2.05 \times 10^{-4}$, 1.11×10^{-4}, and 4.54×10^{-5} m^2/s.

After an initial transient, the exponential growth rate becomes linear and is the slope of the curve of a log of the amplitude versus time plot, where the amplitude of the instability is defined as the average absolute displacement at the bounding edge and line of symmetry at the center of the wave. Numerical results for the three Reynolds numbers using the THINC-EM method are presented in Fig. 6. The dimensionless growth rate is presented versus Reynolds number in Fig. 7. The results compare well with that of Chandrasekhar [30].

7.3. Dam-break problem

Another classical test case is the dam-break problem. In our variation, we follow [11] and consider a 6 m × 1.5 m rectangular domain discretized using a uniformly spaced 480 × 128 cell mesh. Liquid water (ρ_l=1000 kg/m^3, μ_l=1e-3 kg/(m-s)) is placed inside a rectangle extending from X = 0 m to X = 1 m and from Y = 0 m to Y = 1 m. Air (ρ_l = 1.0 kg/m^3, μ_l=1e-5 kg/(m-s)) is located everywhere else, and hydrostatic equilibrium is enforced for the pressure field. The time step is 0.0002 s ($\frac{\Delta x_{\min}}{\Delta t}$ = 80

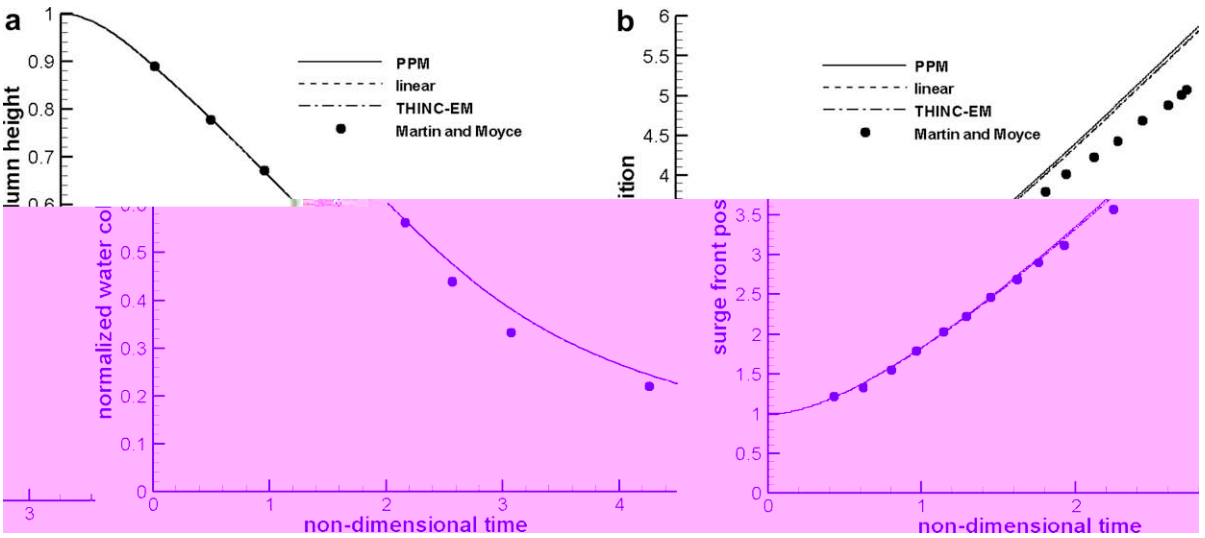

Fig. 8. Predictions of column height (a) and surge (b) for two-dimensional dam-break problem.

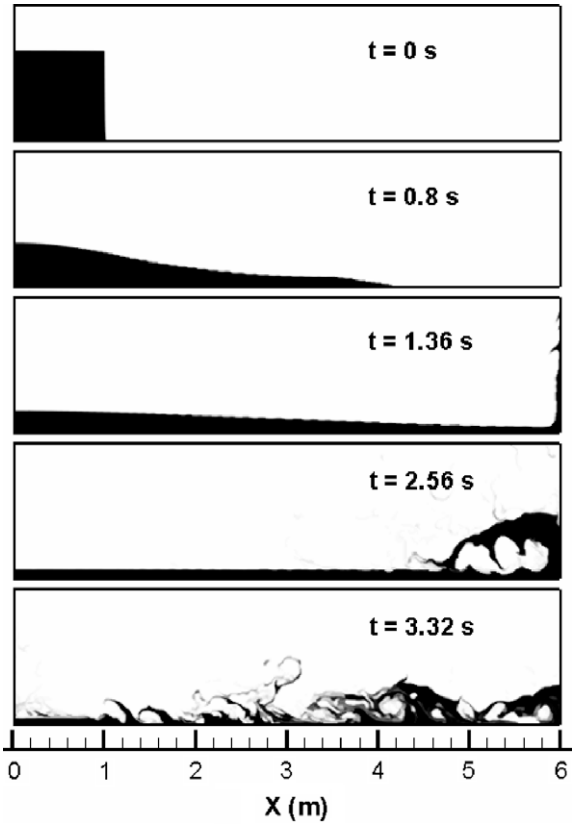

Fig. 9. Time evolution of liquid volume fraction for two-dimensional dam-break problem (THINC-EM).

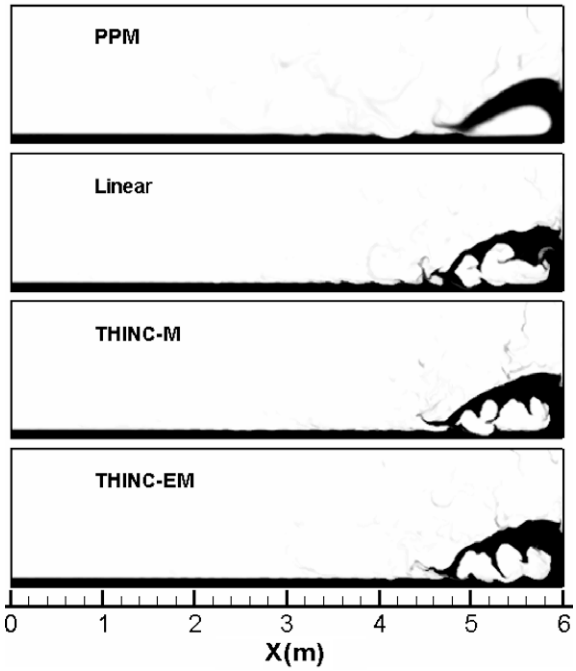

Fig. 10. Effect of different reconstruction schemes ($t = 2.56$ s).

Table 4
Percent mass errors for dam-break problem.

Scheme	Percent mass error (gas)		Percent mass error (liquid)	
	Max	Average	Max	Average
PPM	0.002	0.001	0.015	0.009
Linear	0.010	0.004	0.077	0.036
THINC-M	0.006	0.003	0.044	0.025
THINC-EM	0.006	0.004	0.044	0.028

in Eq. (21)). No-slip boundary conditions are applied on all surfaces. Fig. 8(a) and (b) compare the interface position along the far-left wall and along the bottom wall with data from Martin and Moyce [32]. The interface position is normalized with respect to its initial value (L), while the time is non-dimensionalized by multiplying it by $\sqrt{gL}$, with $g = 9.81$ m/s^2. Good agreement is indicated initially but some deviations appear for later times. These may be the result of insufficient resolution of frictional effects. Fig. 9 presents snapshots of the evolution of the water front at different time instances for the THINC-EM scheme. The liquid volume fraction (45 contours, ranging from 0 to 1) is shown. Weak instabilities present on the surface of the liquid sheet are excited as the colliding water stream detaches from the right side and upper walls, producing a complicated Kelvin–Helmholtz type pattern at later times. Filaments of fluid are periodically detached from the evolving sheets, and several instances of 'mixed-out' regions of fluid becoming more coherent are present at later times. Fig. 10 compares snapshots at $t = 2.56$ s from the PPM, linear, THINC-M, and THINC-EM reconstructions. The PPM reconstruction is clearly more dissipative, while the others display a sharp capturing of the breaking wave. Table 4 shows that the percent mass errors for the gas and liquid phases are less than 0.1% over the 20,000-iteration duration of the calculations. Snapshots from a three-dimensional calculation of the dam-break problem are shown in Fig. 11. The computational domain is extended 0.5 m in the *Z-direction,* and the mesh contains $480 \times 128 \times 21$ cells. The breaking wave displays a clear three-dimensional structure, and the calculation captures the shedding of small pockets of material as the breaking wave 'splashes' onto the incoming stream.

7.4. Axisymmetric jet instability

The next case considered corresponds to calculations of interfacial instability growth along the surface of a liquid jet, exiting into quiescent gas. This case corresponds to that considered computationally by Liang and Ungewitter [33] (though with a much more severe density variation in the present case) in their studies of wind-induced jet instability using volume-of-fluid methods. Chigier and Reitz [34] present an excellent review article that surveys key developments in primary atomization theory. One item emphasized is the use of linear stability analysis to predict the initial growth of instabilities along a

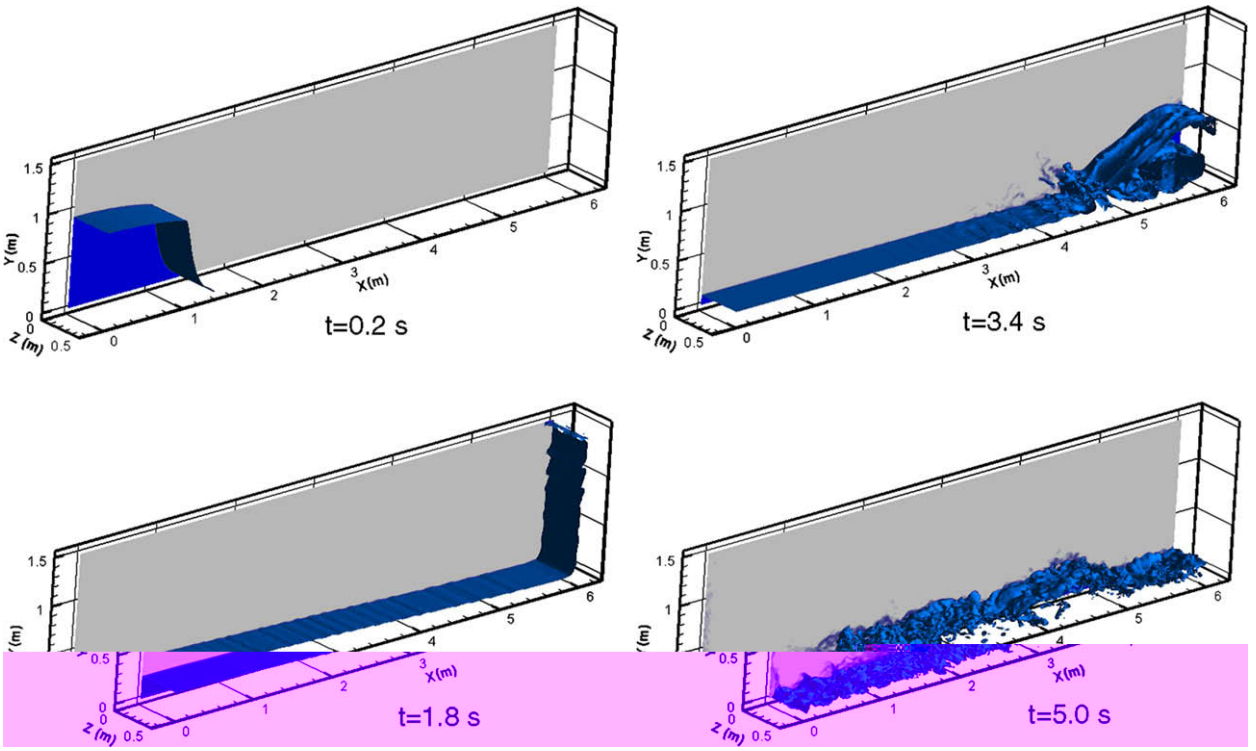

Fig. 11. Isosurfaces of α=05 for three-dimensional dam-break problem (THINC-EM).

phase interface. Such analyses can be conducted under various assumptions, and the most detailed theories consider shear within the gas and liquid phases, as well as the interfacial tension, as driving forces for instability growth. Results are generally correlated in terms of Weber and Ohnesorge numbers, the former representing the ratio of inertial forces to interfacial forces, and the latter representing the ratio of viscous forces to interfacial forces. Many theories for primary atomization use the wavelength of the most amplified disturbance (for fixed Weber and Ohnesorge numbers) as being proportional to the diameter of the droplets that are initially separated from the jet. The dispersion equation governing linear wave growth has been solved numerically by Reitz [35], and the results for wavelength of the most amplified disturbance and its growth rate curve-fitted as functions of Weber and Ohnesorge numbers:

$$\frac{\Lambda}{a} = 9.02\frac{(1+0.45Z^{0.5})(1+0.4(Z\mathrm{We}_v^{0.5})^{0.7})}{(1+0.87\mathrm{We}_v^{1.67})^{0.6}}, \tag{51}$$

where a is the initial jet radius, Λ is the wavelength of the most amplified disturbance, $\mathrm{We}_v = \rho_v U^2 a/\sigma$ is the Weber number based on the gas-phase density and the relative velocity U, $Z = \mathrm{We}_l^{0.5}/Re_l \quad \mathrm{We}_l^{=}\rho_l U^2 a/\sigma$, $Re_l^{=}\rho_l U a/\mu_l$, and σ is the interfacial tension.

The growth rate Ω determines the rate at which an initial perturbation with amplitude η grows in time, assuming an exponential dependence: $\eta(t) = \eta_o \exp(\Omega t)$ with

$$\Omega\left[\frac{\rho_l a^3}{\sigma}\right] = \frac{0.34+0.38\mathrm{We}_v^{1.5}}{(1+Z)(1+1.4(Z\mathrm{We}_v^{0.5})^{0.6}} \tag{52}$$

To test the ability of the schemes to replicate the initial stages of jet instability, a test case involving an axisymmetric water-jet exiting into quiescent air is considered. The domain extends 0.01 m in the *X-direction* and 0.02 m in the *Y-direction* and the jet radius is 0.005 m. Periodic boundary conditions are enforced at X = 0 m and X = 0.01 m, thus simulating the evolution of a temporal disturbance. The velocity of the gas portion is set to zero initially, and the liquid velocity is set to 7.694 m/s. This value corresponds to the solution of Eq. (51) for the case where Z = 0 (inviscid flow) and Λ=2 a=0.01 m. For this case, the growth rate is estimated to be about 100 s^{-1} from Eq. (52). A grid containing 238 × 272 cells, uniformly spaced over a 0.01 × 0.01 domain but stretching vertically to the upper boundary located at Y = 0.02 m is used, and the calculations were evolved at a time step of 3e-6 s ($\frac{\Delta x_{\min}}{\Delta t}$ = 20 in Eq. (21)). The calculations were initialized by specifying the normal velocity component in the liquid jet (Y < 0.005 m) as [33]

$$v(x,y) = 0.001\sin\left(\frac{2\pi}{\mathrm{A}}x\right)\left(\frac{y}{0.005}\right) \tag{53}$$

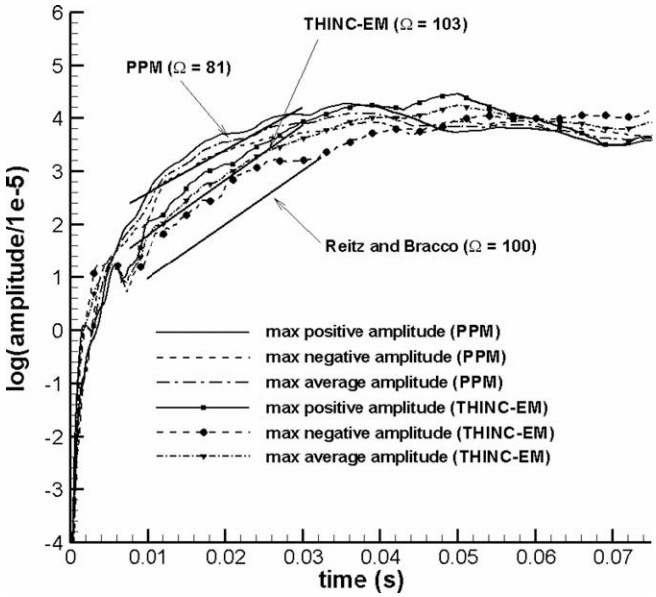

Fig. 12. Normalized disturbance amplitude versus time.

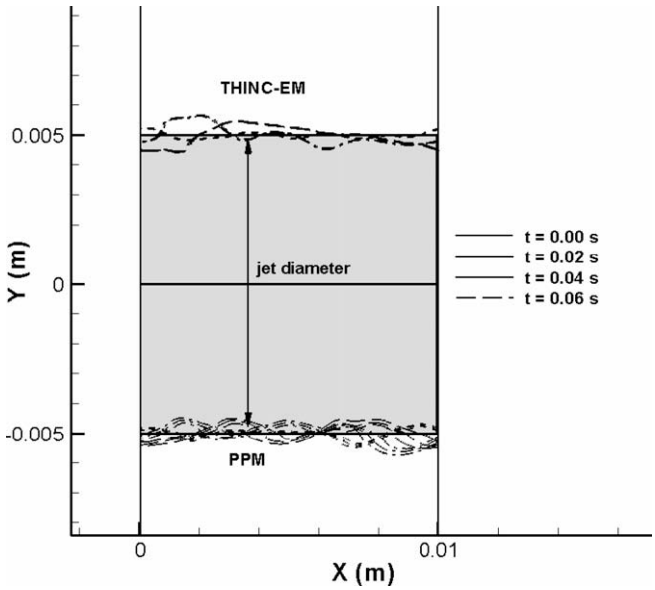

Fig. 13. Evolution of jet surface shape.

Fig. 12 presents normalized amplitudes for the PPM and THINC-EM reconstructions. Calculations performed using the linear and the THINC-M reconstructions diverged. Amplitudes were determined by averaging the maximum and minimum deviations from the nominal interface position at $Y = 0.005$ m as extracted at each time step. The growth rate is the slope of the log of the normalized amplitude; a true linear evolution of the disturbance would yield a constant slope versus time. Asymptotic growth rates (indicated somewhat subjectively by linear curve fitting over the interval from $t = 0.0075$ to $t = 0.03$ s) indicate that the PPM and the THINC-EM results are reasonably close to the theoretical value of 100 s^{-1}. At later times, the growth rate slows for both methods, and the wavelength of the interface disturbance increases. The effect of THINC-EM in maintaining a sharp liquid–vapor interface is shown clearly in Fig. 13, which plots contours of $\alpha = 0.05$, $\alpha = 0.5$, and $\alpha = 0.95$ at several instances in time. The gray shaded region indicates the initial position of the jet. At the last time instance shown, the wave length of the disturbance in the THINC-EM calculation is near the theoretical value of 0.01 m, while it is shorter for the PPM calculation.

7.5. Surface tension – driven instability (Rayleigh problem)

In this case and the next, only the THINC-EM scheme is used. To validate the implementation of the continuum surface force (CSF) model of [26], the evolution of a cylindrical (2D) and a spherical (3D or axisymmetric) water drop in a quiescent fluid is considered. A water drop of radius 0.0025 m is embedded in a quiescent, constant-pressure fluid. The expected response is a rise in the bubble pressure to theoretical values of $p_{\text{drop}} - p_{\infty} = \frac{\sigma}{R_{\text{drop}}}$ for a cylindrical drop and $p_{\text{drop}} - p_{\infty} = 2\frac{\sigma}{R_{\text{drop}}}$ for a spherical drop. Fig. 14 shows that the theoretical result is reached in all cases and remains approximately constant over time. As is common for a CSF model, 'parasitic velocity currents' [26] are observed in all cases, but these perturbations do not amplify to the point that the calculation is destabilized and the structure of the bubble is disrupted.

Chandrasekhar [30] presents an analytic solution to the Rayleigh problem involving the evolution of a surface instability on an axisymmetric cylindrical jet due to surface-tension effects. The initial amplitude, A_0, of the disturbance will increase with time due to surface tension, σ, according to the relation $A = A_0 e^{n^* t}$, where n^* is the growth rate. The analytic solution is

$$n^{*2} = \frac{\sigma}{a^3 \rho} \frac{k\mathrm{I}_1(\mathrm{k})}{\mathrm{I}_0(\mathrm{k})}\left(1 - k^2\right), \tag{54}$$

where $\mathrm{I}_1(\mathrm{k})$ and $\mathrm{I}_0(\mathrm{k})$ are modified Bessel functions, a is the jet radius and ρ is the density of the liquid. The solution is normalized, resulting in a dimensionless growth rate, $n = n^*/\sqrt{\sigma/(a^3\rho)}$, for a given dimensionless wave number $k = k^* a$, where the wave number $k^* = 2\pi/\Lambda$.

In the present work, an axisymmetric cylindrical water-jet of radius $a = 0.001\ m$ is placed in a domain of radius $l = 3a$ and varying axial length Λ, the remainder being filled with air. The profile of an initial perturbation of the water-jet surface given as

$$\phi = a - r - A_0 \cos(2\pi x/\Lambda) \tag{55}$$

where ϕ is the interface location and $A_0 = 0.01a$. The initial velocity is set to zero, and the initial pressure is constant. The grid consists of 101 radial nodes and a varying number of axial nodes (depending on Λ) with $\Delta x = \Delta r$. A symmetric boundary condition is used at the axis of the jet, a constant-pressure condition is enforced at the $r = l$ boundary, and periodic boundary conditions are applied at $x = 0$ and $x = \Lambda$, following the numerical work of Menard et al. [13].

Qualitative predictions of the time history of the instability, showing the eventual breakup of the jet, are presented in Fig. 15 for $\Lambda = 4a = 0.004\ m$. Fig. 16 presents a comparison of the predicted disturbance growth rate with the analytic solution of Eq. (54). Dimensionless wave numbers were varied by holding the radius of the jet constant while varying the length of the jet. The computational results are in close agreement with the analytic solution for each of the five wave numbers.

7.6. 'In–out' aerated-liquid injector

The last test case considered in this study involves flow within an aerated-liquid (or 'barbotage') fuel injector. Devices of this type have been tested at the Air Force Research Laboratory for use in accelerating primary jet breakup in hydrocarbon-fueled scramjet engines. A schematic of an 'in–out' injector, in which aerating gas is injected through a central tube into a co-flowing liquid stream, is shown in Fig. 17. The specific configuration considered [36] injects nitrogen gas through the end

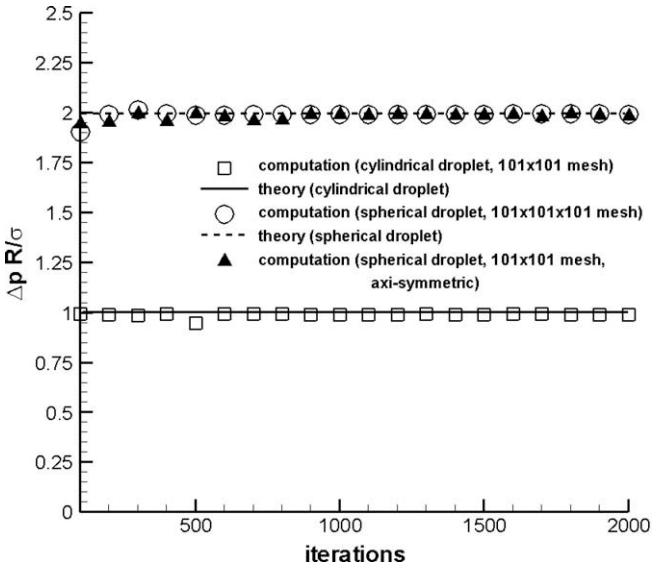

Fig. 14. Normalized droplet pressure versus time – static drop calculation (THINC-EM).

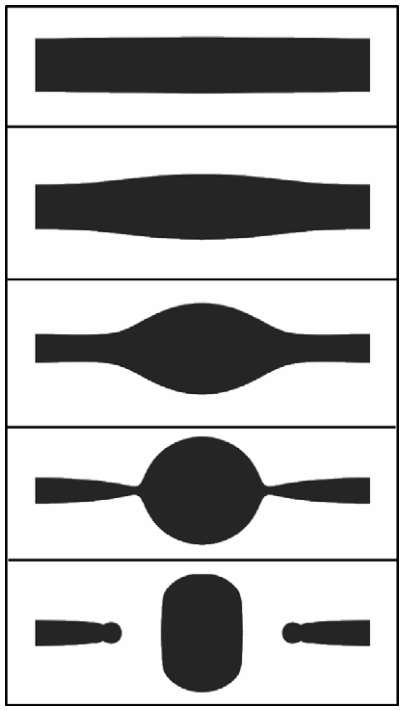

Fig. 15. Time evolution of jet surface (Rayleigh instability; THINC-EM).

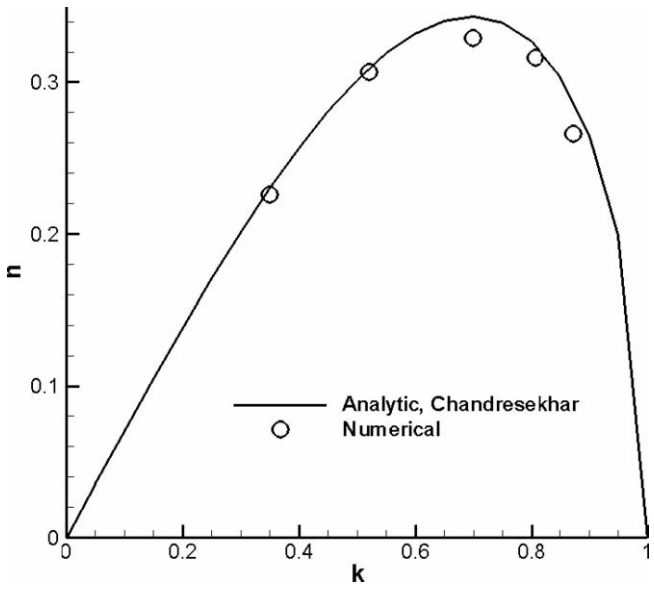

Fig. 16. Dispersion relation for Rayleigh instability (THINC-EM).

of the tube, rather than through an array of holes as shown in the schematic. The operation of an aerated-liquid injector of this type is parameterized by the gas-to-liquid mass ratio (GLR). Low values of the GLR (0.15% or less) result in the intermittent passage of slugs of gas and liquid through the injector. Higher values lead to a core-annular flow structure in which the aerating gas pushes the liquid toward the walls of the discharge tube. Both situations have been simulated numerically using a compressible two-phase mixture model [25]. In the present work, we adopt the incompressible flow model described above to simulate a case for which the GLR is approximately 0.115%. Inlet gas velocities for the two cases are 2.34 m/s and 4.69 m/s, and the liquid injection velocity is initially set to 0.586 m/s. Bernoulli-inflow boundaries are applied at the liquid water inlet, whereas a fixed volume flow rate is applied at the inlet of the gas injection tube. The actual inflow

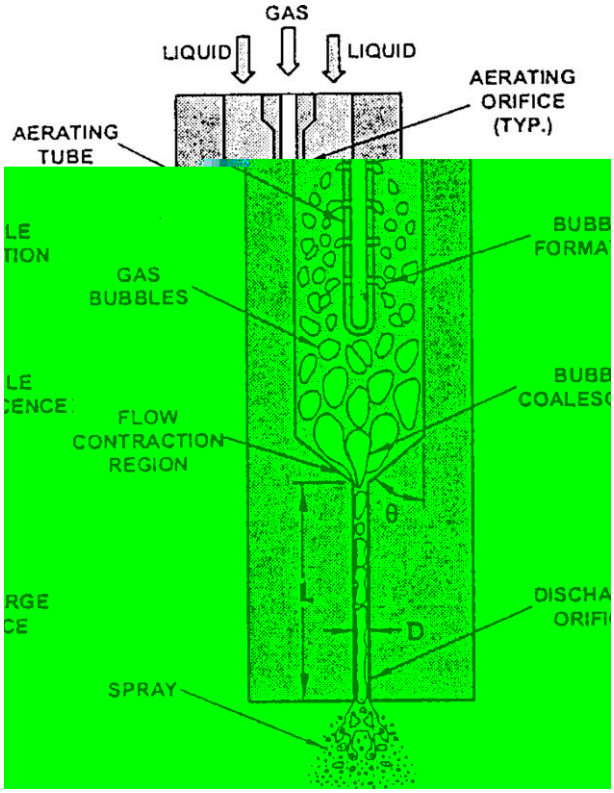

Fig. 17. Schematic of 'in–out' aerated-liquid injector (from Ref. [36]).

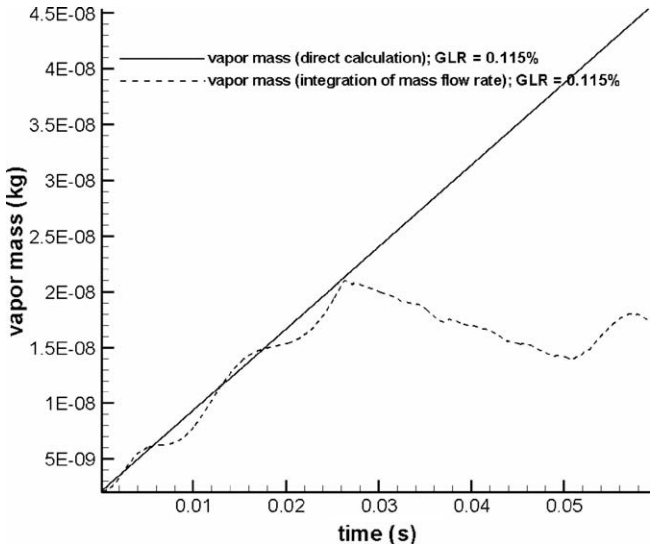

Fig. 18. Evolution of vapor mass within 'in–out' aerated-liquid injector (THINC-EM).

conditions for the liquid jet (and thus the GLR value) will evolve over time. A two-dimensional analogue of the three-dimensional injector described in [36] is used, with the circular tube replaced by a slot. The mesh contains 294,000 interior mesh cells, distributed over 30 blocks. The calculations were evolved at a time step of 1e-6 s ($\frac{\Delta x_{\min}}{\Delta t}$=20 in Eq. (21)) for a period of 0.06 s using the THINC-EM scheme.

Fig. 18 compares the vapor mass within the system to the value resulting from the time integration of the vapor mass flow rate. A perfect correlation should be achieved prior to the exiting of the first slug of vapor from the tube. This does

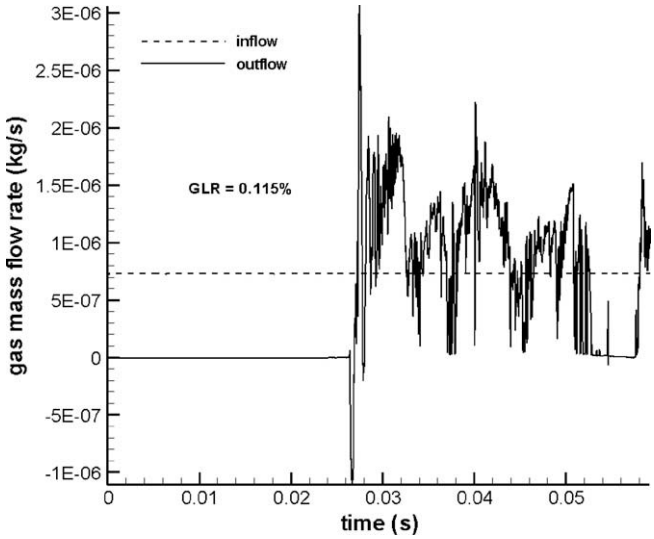

Fig. 19. Mass flow rates versus time in 'in–out' aerated-liquid injector (THINC-EM).

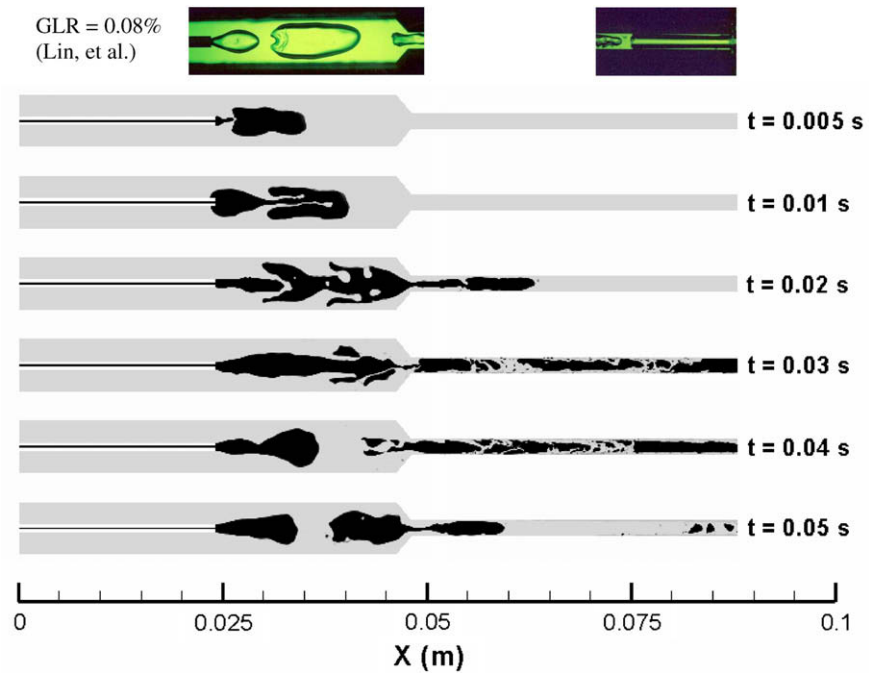

Fig. 20. Evolution of vapor volume fraction in 'in–out' aerated-liquid injector (GLR = 0.115%, THINC-EM).

not happen exactly, as discrete bubble-collapse events induce very high velocities (~60 m/s) that limit the ability of the time-advancement method to converge the sub-iterations properly. Fig. 19 presents inlet and outlet vapor mass flow rates versus time. The outflow mass flow rate shows features characteristic of a core-annular structure in the initial response and a slugging response at later times. Fig. 20 presents discrete snapshots of vapor volume fraction. Bubbles are initially formed in the relatively slow-moving fluid upstream of the discharge tube. These progress rapidly through the discharge tube and are deformed and fragmented by shearing stresses. At later times, the bubble shapes are qualitative agreement with images for GLR ~0.08% from [34]. The predicted bubble shapes are not as rounded as those observed in the images. This might be attributed to the relative reduction in surface-tension force in the two-dimensional calculation, the presence of side walls in the experiment, and differences in slot injection (modeled) versus injection through a round orifice.

8. Conclusions

Several algebraic interface-sharpening techniques, suitable for incorporation as part of a dimension-by-dimension MUSCL-type upwinding strategy, have been derived and studied in this work. Linear and sine-wave reconstructions of the volume fraction within a mesh cell have been developed, as have modified versions of the Tangent Hyperbola for interface-capturing (THINC) scheme of Xiao et al. [16]. Techniques for blending the sharpening strategies with a baseline Piecewise Parabolic Method (PPM) [29] reconstruction have also been presented. The schemes have been incorporated into an incompressible Navier–Stokes solver that uses a variant of Chorin's artificial compressibility method to solve the equations in their time-dependent form and uses a low-diffusion flux-splitting scheme for spatial discretization of the inviscid fluxes. Accurate results have been obtained for moving discontinuities, the Rayleigh–Taylor instability, a dam-break problem, an axisymmetric jet instability, the Rayleigh instability, and flow within an 'in–out' aerated-liquid injector. The linear and modified THINC reconstructions, implemented in a conventional MUSCL-type manner, provide very sharp resolution of volume-fraction discontinuities but sometimes induce 'stair-stepping' behavior. The modified THINC reconstruction, implemented using exact integration of the flux of material crossing a mesh cell, provides a slightly more diffusive capturing of phase interfaces and is nearly as robust as the baseline PPM reconstruction. This model appears quite suitable for further evaluation and testing.

Acknowledgments

This work has been partially supported by Taitech, Incorporated under Contract T002-34-01, by the Office of Naval Research under Grant N000140510224, and by MeadWestvaco Corporation under Task Order 2008-0783. Computer resources have been provided by the High Performance Computing component of NC State's Information Technologies Division (www.ncsu.edu/itd/hpc).

References

[1] C.W. Hirt, A.A. Amsden, J.L. Cook, An arbitrary Lagrangian–Eulerian computing method for all flow speeds, Journal of Computational Physics 135 (1997) 203–216.
[2] S.O. Unverdi, G. Tryggvason, A front-tracking method for viscous, incompressible, multi-fluid flow, Journal of Computational Physics 100 (1992) 25–37.
[3] S. Popinet, S. Zaleski, A front-tracking algorithm for accurate representation of surface tension, International Journal for Numerical Methods in Fluids 30 (1999) 775–793.
[4] C.W. Hirt, B.D. Nichols, Volume of fluid (VOF) methods for the dynamics of free boundaries, Journal of Computational Physics 39 (1981) 201–225.
[5] O. Ubbink, R.I. Issa, A method for capturing sharp fluid interfaces on arbitrary meshes, Journal of Computational Physics 153 (1999) 26–50.
[6] E. Puckett, A. Almgren, J. Bell, D. Marcus, W. Rider, A high-order projection method for tracking fluid interfaces in variable density incompressible flows, Journal of Computational Physics 130 (1997) 269–282.
[7] J. Pilliot, E.G. Puckett, Second order accurate volume-of-fluid algorithms for tracking material interfaces, Journal of Computational Physics 199 (2004) 465–502.
[8] S. Osher, J.A. Sethian, Fronts propagating with curvature dependent speed: algorithms based on Hamilton–Jacobi formulations, Journal of Computational Physics 79 (1988) 12–49.
[9] M. Sussman, E. Fatemi, An efficient interface preserving level set re-distancing algorithm and its application to interfacial incompressible fluid flow, SIAM Journal on Scientific Computing 20 (1999) 1165–1191.
[10] M. Sussman, E.G. Puckett, A coupled level set and volume of fluid method for computing 3D and axisymmetric incompressible two-phase flows, Journal of Computational Physics 162 (2000) 301–337.
[11] E. Marchandise, J.-F. Remancle, A stabilized finite element method using a discontinuous level set approach for solving two-phase incompressible flows, Journal of Computational Physics 219 (2006) 780–800.
[12] R. Fedkiw, T. Aslam, B. Merriman, S. Osher, A non-oscillatory Eulerian approach to interfaces in multimaterial flows (the Ghost fluid method), Journal of Computational Physics 152 (1999) 457–492.
[13] T. Menard, S. Tanguy, A. Berlemont, Coupling level set/VOF/Ghost fluid methods: validation and application to 3D simulation of the primary break-up of a liquid jet, International Journal of Multiphase Flow 33 (2007) 510–524.
[14] R.R. Nourgaliev, T.N. Dinh, T.G. Theofanous, A pseudocompressibility method for the numerical solution of incompressible multifluid flows, International Journal of Multiphase Flow 30 (2004) 6901–6937.
[15] D. Pan, C.-H. Chang, The capturing of free surfaces in incompressible multi-fluid flows, International Journal for Numerical Methods in Fluids 33 (2000) 203–222.
[16] F. Xiao, Y. Honma, T. Kono, A simple algebraic interface-capturing scheme using hyperbolic tangent function, International Journal of Numerical Methods in Fluids 48 (2005) 1023–1040.
[17] K. Yokoi, Efficient implementation of THINC scheme: a simple and practical smoothed VOF algorithm, Journal of Computational Physics 226 (2007) 1985–2002.
[18] A.J. Chorin, A numerical method for solving incompressible Navier–Stokes equations, Journal of Computational Physics 2 (1967) 12–26.
[19] J.R. Edwards, Towards Unified CFD Simulations of Real Fluid Flows, AIAA Paper 2001-2524CP, June 2001, unpublished.
[20] M.D. Neaves, J.R. Edwards, All-speed time-accurate underwater projectile calculations using a preconditioning algorithm, Journal of Fluids Engineering 128 (2006) 284–296.
[21] M.S. Liou, A sequel to AUSM, Part II, AUSM+-UP for all speeds, Journal of Computational Physics 214 (2006) 137–170.
[22] J.W. Lindau, S. Venkateswaran, R.F. Kunz, C.W. Merkle, Development of a Fully Compressible Multi-Phase Reynolds-Averaged Navier–Stokes Model, AIAA Paper 2001-2648, June 2001, unpublished.
[23] J.R. Edwards, M.-S. Liou, Simulation of Two-phase Flows Using Low-Diffusion Shock-capturing Schemes, AIAA Paper 2006-1288, June 2006, unpublished.
[24] M. Tian, X. Xiao, J.R. Edwards, K.-C. Lin, T.A. Jackson, Numerical Simulation and Experimental Characterization of the Internal Two-Phase Flow within an Aerated Liquid Injector, AIAA Paper 2004-2645, June 2004, unpublished.
[25] M. Tian, J.R. Edwards, K.-C. Lin, T.A. Jackson, Numerical Simulation of Transient Two-Phase Flow within Aerated-Liquid Injectors, AIAA Paper 2003-4226, June 2003, unpublished.
[26] B. LaFaurie, C. Nardone, R. Scardovelli, S. Zaleski, G. Zanetti, Modelling merging and fragmentation in multiphase flows with SURFER, Journal of Computational Physics 113 (1994) 134–147.

[27] M. Choudhari, M. Khorrami, J.R. Edwards, Computational Study of Micro-Fluid Mechanics of Duct Acoustic Treatment, AIAA Paper 1999-1851, May 1999, unpublished.
[28] S. Venkateswaran, C.L. Merkle, Efficiency and Accuracy Issues in Contemporary CFD Algorithms, AIAA Paper 2000-2251, June 2000, unpublished.
[29] P. Colella, P.R. Woodward, The piecewise parabolic method (PPM) for gas-dynamical simulations, Journal of Computational Physics 54 (1984) 174–201.
[30] S. Chandrasekhar, Hydrodynamic and Hydromagnetic Stability, Oxford University Press, London, 1961.
[31] B.J. Daly, Numerical study of two fluid Rayleigh–Taylor instability, The Physics of Fluids 10 (1967) 297–307.
[32] J. Martin, W. Moyce, An experimental study of the collapse of liquid columns on a rigid horizontal plane, Philosophical Transactions A 244 (1952) 312–324.
[33] P.Y. Liang, R.J. Ungewitter, Modeling of atomization and secondary breakup from first principles, in: Kenneth K. Kuo (Ed.), Recent Advances in Spray Combustion: Spray Atomization and Drop Burning Phenomena, vol. I, in: Paul Zarchan (Editor-in-Chief), Progress in Astronautics and Aeronautics, vol. 166, AIAA, Reston, Va., 1996, pp. 481–504.
[34] N. Chigier, R.D. Reitz, Regimes of jet breakup and breakup mechanisms (physical aspects), in: Kenneth K. Kuo (Ed.), Recent Advances in Spray Combustion: Spray Atomization and Drop Burning Phenomena, vol. I, in: Paul Zarchan (Editor-in-Chief), Progress in Astronautics and Aeronautics, vol. 166, AIAA, Reston, Va., 1996, pp. 109–160.
[35] R.D. Reitz, Modeling atomization process in high-pressure vaporizing sprays, Atomization and Spray Technology 3 (1987) 309–337.
[36] K.-C. Lin, P.J. Kennedy, T.A. Jackson, Structures of Internal Flow and the Corresponding Spray for Aerated-Liquid Injectors, AIAA Paper 2001-3569, June 2001, unpublished.